Finite-sized gas bubble motion in a blood vessel: Non-Newtonian effects

Karthik Mukundakrishnan,[1,2] Portonovo S. Ayyaswamy,[2,*] and David M. Eckmann[1]
[1]*Department of Anesthesiology and Critical Care, University of Pennsylvania, Philadelphia, Pennsylvania, 19104, USA*
[2]*Department of Mechanical Engineering and Applied Mechanics, University of Pennsylvania, Philadelphia, Pennsylvania 19104, USA*
(Received 16 April 2008; revised manuscript received 30 June 2008; published 5 September 2008)

We have numerically investigated the axisymmetric motion of a finite-sized nearly occluding air bubble through a shear-thinning Casson fluid flowing in blood vessels of circular cross section. The numerical solution entails solving a two-layer fluid model—a cell-free layer and a non-Newtonian core together with the gas bubble. This problem is of interest to the field of rheology and for gas embolism studies in health sciences. The numerical method is based on a modified front-tracking method. The viscosity expression in the Casson model for blood (bulk fluid) includes the hematocrit [the volume fraction of red blood cells (RBCs)] as an explicit parameter. Three different flow Reynolds numbers, $\mathrm{Re}_{\mathrm{app}}=\rho_l U_{\max} d/\mu_{\mathrm{app}}$, in the neighborhood of 0.2, 2, and 200 are investigated. Here, ρ_l is the density of blood, $U_{\max}$ is the centerline velocity of the inlet Casson profile, d is the diameter of the vessel, and μ_{app} is the apparent viscosity of whole blood. Three different hematocrits have also been considered: 0.45, 0.4, and 0.335. The vessel sizes considered correspond to small arteries, and small and large arterioles in normal humans. The degree of bubble occlusion is characterized by the ratio of bubble to vessel radius (aspect ratio), λ, in the range $0.9 \leqslant \lambda \leqslant 1.05$. For arteriolar flow, where relevant, the Fahraeus-Lindqvist effects are taken into account. Both horizontal and vertical vessel geometries have been investigated. Many significant insights are revealed by our study: (i) bubble motion causes large temporal and spatial gradients of shear stress at the "endothelial cell" (EC) surface lining the blood vessel wall as the bubble approaches the cell, moves over it, and passes it by; (ii) rapid reversals occur in the sign of the shear stress $(+ \rightarrow - \rightarrow +)$ imparted to the cell surface during bubble motion; (iii) large shear stress gradients together with sign reversals are ascribable to the development of a recirculation vortex at the rear of the bubble; (iv) computed magnitudes of shear stress gradients coupled with their sign reversals may correspond to levels that cause injury to the cell by membrane disruption through impulsive compression and stretching; and (v) for the vessel sizes and flow rates investigated, gravitational effects are negligible.

DOI: 10.1103/PhysRevE.78.036303 PACS number(s): 47.55.dd, 47.50.−d, 47.63.Cb, 47.61.Jd

I. INTRODUCTION

Air embolism in the cardiopulmonary system has been a subject of interest to clinicians and researchers for many years because of the severe hemodynamic and gas exchange abnormalities that result [1]. Many studies of air embolism have been done in the context of decompression illness, which is a prominent problem for divers but may affect aviators and astronauts as well. The intravascular gas emboli may deposit into organs, such as the heart or the brain, and as a result, cause permanent injury. Recent study has shown that the distribution of gaseous emboli in the pulmonary blood vessels is influenced not only by their differential density from blood (buoyancy) but also by the flow dynamics within the pulmonary vascular tree [2]. The simplest possible representation of an intravascular gas embolus is the pressure-driven motion of a bloodlike fluid in a circular vessel containing a bubble of comparable diameter. For the past several years, we have been experimentally and numerically investigating bubble motion in liquid filled cylinders in the context of pulmonary gas embolism ([3–8]). When the size of the bubble is comparable to the vessel diameter, which is often the case in gas embolism, the confining walls affect the bubble shape and in turn its mobility. Calculating the dynamics of such a bubble requires numerical solutions of the Navier-Stokes equations governing the motion of fluid in both the gas and bulk fluid (blood) phases that are typically characterized by large jumps in fluid properties, namely, density and viscosity, in addition to the presence of high surface tension forces. This problem is further complicated by the presence of fluid inertia in the bulk phase and the fact that blood is a rheologically complex fluid [9].

A number of experimental and modeling studies of problems somewhat related to the topic under discussion have been reported in the literature (see [10–29]). To the best of our knowledge, at present, there are no studies available that have considered the biofluid mechanics of a finite-sized gas bubble moving through a rheologically complex fluid for a wide range of Reynolds numbers that are encountered in typical arterial flows. In this paper, we present a rigorous mathematical formulation and numerical solutions for the axisymmetric motion of a finite-sized occluding gas bubble moving in a blood vessel.

There are a number of numerical methods that are available for investigating the problem under consideration (see [20,27,30–42]). After considerable numerical experimentation, we have chosen to employ an immersed boundary front-tracking scheme [30]. The scheme has been modified to include a level contour reconstruction procedure for periodic

*Author to whom correspondence should be addressed. Present address: Department of Mechanical Engineering and Applied Mechanics, 229 Towne Building, 220 S. 33rd Street, University of Pennsylvania, Philadelphia, Pennsylvania 19104. ayya@seas.upenn.edu

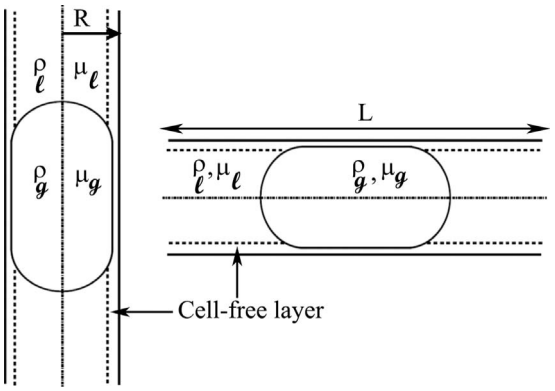

FIG. 1. Schematic of a nearly occluding bubble in vertical and horizontal vessel configurations.

reconstruction of the front and a "density-weighted" surface tension force distribution scheme [7].

Our study is particularly focused on evaluating the bubble shape, mobility, and importantly, the wall shear stress and the residence time for the bubble in the vicinity of an "endothelial cell" (EC) lining the vessel interior. For evaluating the wall shear stress, a typical point on the cell surface is considered. For the residence time, the time duration for bubble transit across a typical endothelial cell length is considered.

The paper is organized as follows. First, a mathematical description of the problem is provided with necessary boundary and initial conditions. Then the numerical method employed to solve the problem is presented. It is then followed by results and discussion. The final section deals with the major conclusions of the present study.

II. MATHEMATICAL FORMULATION

A. Governing equations

We consider the axisymmetric motion of a gas bubble in a vessel of circular cross section of radius R (diameter d) as shown in Fig. 1. The vessel configuration may be vertical or horizontal. The gas bubble may be spherical or elongated. For the nearly spherical occluding bubble, the aspect ratio λ (radius of the bubble to the radius of the vessel) could be near unity ($\lambda < 1$). For an elongated occluding bubble, the aspect ratio λ may be equal to or larger than unity ($\lambda \geqslant 1$) and in this case at introduction, a thin annular film between the bubble and the vessel wall is taken to surround the bubble. It should be noted that for an elongated occluding bubble, the equivalent spherical bubble will have a radius equal to or exceeding that of the vessel. The instantaneous shape of the bubble will depend on the prevailing flow conditions.

The gas is assumed incompressible with density ρ_g and viscosity μ_g. The bulk fluid is also incompressible and modeled as a shear-thinning Casson fluid of viscosity μ_l and density ρ_l. Note that μ_l is a spatially varying parameter and depends on the local shear rate.

The equations of motion for the two-phase flow (bubble +blood) may be expressed as

$$\nabla \cdot \mathbf{u} = 0, \tag{1}$$

$$\rho\left(\frac{\partial \mathbf{u}}{\partial t} + \nabla \mathbf{u} \cdot \mathbf{u}\right) = -\nabla p + \nabla \cdot \mu(\nabla \mathbf{u} + \nabla^T \mathbf{u}) + \int_{S(t)} \sigma \mathcal{K} \mathbf{n}_f \hat{\delta}(\mathbf{x} - \mathbf{x}_f) ds + \rho \mathbf{g}. \tag{2}$$

Here, $\mathbf{u} \equiv (v_r, v_z)$ is the fluid velocity, v_r, v_z are the velocity components along the radial and axial directions, p is pressure, ρ and μ are the density and viscosity of the medium (defined below), $\mathbf{g}$ is gravitational acceleration (=0 for a horizontal vessel), s is an arc length measure on the interface, $\mathcal{K}$ is the curvature of the interface, σ is the constant surface tension coefficient, and $S(t)$, $\mathbf{n}_f$, and $\mathbf{x}_f$ denote the instantaneous location of the interface, the unit normal vector on the interface (pointing into the bulk fluid), and the position vector on the interface. $\hat{\delta}(\mathbf{x}-\mathbf{x}_f)$ is the 2D axisymmetric delta function which is nonzero only when $\mathbf{x}=\mathbf{x}_f$. The density and viscosity of the medium are

$$\rho(r,z,t) = \rho_l \mathcal{H}(r,z,t) + \rho_g[1 - \mathcal{H}(r,z,t)], \tag{3}$$

$$\mu(r,z,t) = \mu_l \mathcal{H}(r,z,t) + \mu_g[1 - \mathcal{H}(r,z,t)]. \tag{4}$$

Here, t is time, and $\mathcal{H}(r,z,t)$ is a Heaviside function such that

$$\mathcal{H}(r,z,t) = \begin{cases} 1 & (r,z,t) \text{ in the bulk} \\ 0 & (r,z,t) \text{ in the bubble.} \end{cases} \tag{5}$$

The bulk fluid is modeled as a two-layer fluid consisting of a cylindrical core of concentrated red blood cell (RBC) suspension surrounded by a less viscous, thin cell-free layer. The cell-free layer is modeled as a Newtonian fluid of constant viscosity $\mu_{\text{layer}} = \beta \mu_p$ [43]. Here, μ_p is the plasma viscosity (=1.2 cP). The factor β depends on the thickness of the cell-free layer δ and the core hematocrit H_C. The concentrated suspension of RBCs is modeled as a shear-thinning Casson fluid. Thus, we let

$$\mu_l(r,z,t) = \begin{cases} \mu_c, & 0 \leqslant r \leqslant (1-\delta)R \\ \mu_{\text{layer}}, & (1-\delta)R < r \leqslant R, \end{cases} \tag{6}$$

where δ represents the nondimensional thickness of the cell-free layer normalized with respect to the vessel radius R. The Casson viscosity μ_c is given by (see [44])

$$\mu_c = \left[\sqrt{\mu_\infty} + \sqrt{\frac{\tau_y}{|\dot{\gamma}|}}\right]^2, \tag{7}$$

where τ_y, μ_∞, and $|\dot{\gamma}|$ are the yield stress, the asymptotic Newtonian viscosity, and the shear rate, respectively. For blood, μ_∞ and τ_y are functions of the discharge hematocrit (H_D), the percentage of blood volume made up by red blood cells, and the vessel size. The difficulty in using the Casson model in a numerical scheme lies in its discontinuous character in the limit of zero shear rate ($|\dot{\gamma}| \to 0$). This discontinuity can be overcome by using a regularization technique given in [45]. Following [45], the Casson equation (7) can be recast as

TABLE I. Calculated values of δ, β, and H_C for various H_D's.

H_D	d (μm)	δ	β	H_C	$\mu_{\text{layer}}=\beta\mu_p$ (cP)
0.335	40	0.26	1.3	0.44	1.55
0.335	100	0.1	1.3	0.35	1.55
0.335	2000	0.004	1	0.335	1.2
0.4	40	0.2	1.36	0.5	1.63
0.4	100	0.09	1.39	0.42	1.67
0.4	2000	0.004	1	0.4	1.2
0.45	40	0.2	1.4	0.55	1.69
0.45	100	0.08	1.45	0.47	1.74
0.45	2000	0.004	1	0.45	1.2

$$\mu_c = \left[\sqrt{\mu_\infty} + \sqrt{\frac{\tau_y}{|\gamma|}}(1 - e^{-\sqrt{m|\gamma|}}) \right]^2, \tag{8}$$

where m is the Casson viscosity regularization exponent and is typically taken to be $\sim$100. At spatial locations where $|\gamma|$ is identically equal to zero, a cutoff value for viscosity μ_c =25 cP is chosen on the basis of numerical experimentations carried out as part of the present study. These numerical experimentations included setting μ_c=20 and μ_c=50 cP on the bubble dynamics. The shear rate involves the second invariant of the rate of deformation tensor and is given by

$$|\gamma| = \sqrt{2\,\text{tr}(\mathbf{D}^2)}, \tag{9}$$

$$\mathbf{D} = \frac{\nabla\mathbf{u} + \nabla\mathbf{u}^T}{2}. \tag{10}$$

In Eq. (9), tr($\mathbf{D}^2$) is the second invariant of the rate of deformation tensor $\mathbf{D}$.

In Eq. (8), μ_∞ and τ_y as functions of core hematocrit H_C are given in [46] as

$$\mu_\infty = \frac{\mu_p}{(1-H_C)^{C_1}}, \quad \tau_y^{1/2} = C_2\left[\left(\frac{1}{1-H_C}\right)^{C_1/2} - 1\right]. \tag{11}$$

Here, C_1, C_2 for human blood are 2.0 and 0.3315. The evaluations of the above equations require H_C, δ, and β. In regard to the hematocrit, the discharge hematocrit H_D is usually a known quantity. For $\delta>0$, the core hematocrit H_C, which is based upon the core volume, is larger than H_D. For a given vessel size, the relationships between H_D, H_C, δ, and β are nonlinear. For vessels of diameter in the range 20 μm$\leqslant d \leqslant$300 μm, Sharan and Popel [43] have described methods that are based on nonlinear coupled differential equations supplemented by experimental data. These methods establish relationships between H_D, H_C, δ, and β for known values of d and H_D. We have solved these equations for d=40 μm (small arteriole) and 100 μm (large arteriole) for H_D=0.45, 0.4, and 0.335, and have documented H_C, δ, and β. The details of the Sharan and Popel model are not included here for the sake of brevity. In this study we have also examined a vessel size d=2000 μm (small artery). At such high radius, $\delta\to 0$ and $H_C\sim H_D$. Table I provides these quantities used in our simulations. The following steps are needed for the numerical study:

(1) Determination of core viscosity.

(2) Determination of fully developed velocity profile at the inlet of the vessel using a two-layer model (no bubble).

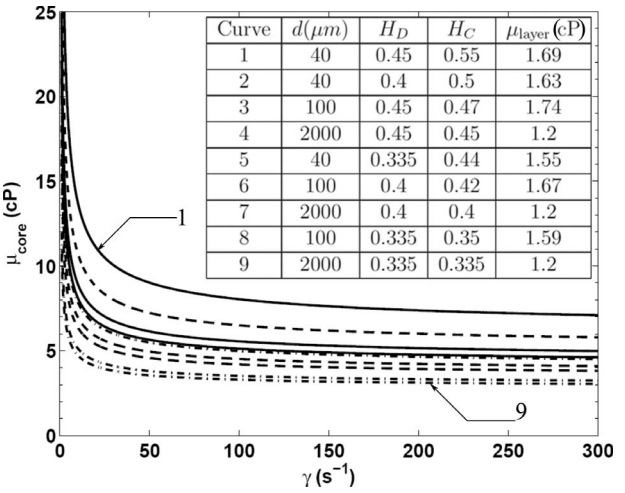

FIG. 2. Core viscosity variation as a function of shear rate for three different discharge hematocrits and vessel sizes. Curve numbering starts from 1 at the top to 9 at the bottom. 1 cP=10^{-2} P =10^{-2} dyn s/cm^2.

B. Core viscosity determination

At a given temperature, the viscosity of blood depends on the viscosity of plasma and its protein content, the hematocrit, the shear rate, and the narrowness of the vessel in which it is flowing. The dependence on the latter is the Fahraeus-Lindqvist effect. The dependence on the prevailing shear rate and the Fahraeus-Lindqvist effect each classify blood as a non-Newtonian fluid.

With inputs from Table I and Eq. (8), we can discern the variation of core viscosity, μ_c as a function of shear rate for various values of H_D, and vessel sizes. These variations are plotted in Fig. 2. The values for H_C are also displayed. For given H_D and γ values, μ_c is the highest for the smallest vessel. For given γ and vessel size values, μ_c is the highest for the largest H_D. For a given H_D and vessel size, the core viscosity varies nonlinearly with γ and sharply increases in the region $0<\gamma<50$. For each H_D, μ_c asymptotes to a constant value at high shear rates. From Fig. 3, the apparent viscosity μ_{app} as defined by Eq. (12) (see [47]) is noted to decrease with vessel diameter for large values of γ (γ >200 s^{-1}) and every H_D.

$$\mu_{\text{app}} = \mu_{\text{layer}}\left[1 - (1-\delta)^4\left(1 - \frac{\mu_{\text{layer}}}{\mu_c}\right)\right]^{-1}. \tag{12}$$

C. Fully developed flow of a Casson fluid without the gas bubble: Two-layer model

By solving the formulation for a fully developed flow in a vessel of a given size, we establish the pressure drop and the

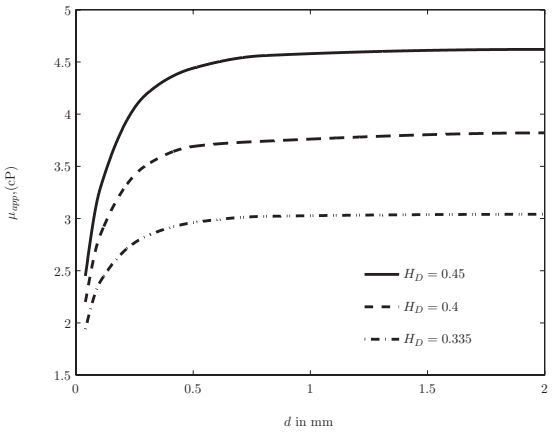

FIG. 3. Apparent viscosity variation as a function of vessel diameter for three H_D's.

velocity profile. The maximum flow velocity is the centerline velocity in the absence of a bubble, $U_{\max}=U_{\text{centerline}}$. This value is known from experiments for normal human blood (hematocrit ~0.4) for the three vessel sizes studied here: a 40-μm-diameter small arteriole, 100-μm-diameter large arteriole, and 2000-μm-diameter small artery. The corresponding values of $U_{\max}$ are listed in Table II. To estimate the corresponding pressure drop (dP/dz) and evaluate the inlet velocity profile, we solve a two-fluid model given by

$$\frac{1}{r}\frac{d}{dr}(r\tau)=\frac{dP}{dz}, \tag{13}$$

where $\tau=\mu_l(dv_z/dr)$, v_z is the axial component (with $U_{\max}=v_z|_{r=0}$), μ_l is given by Eq. (6), and $\gamma=dv_z/dr$. This is subject to $v_z=0$ at $r=R$ (no slip), $\mu_c(dv_z/dr)=\mu_{\text{layer}}(dv_z/dr)$ at $r=(1-\delta)R$ (continuity of shear stress across the core and cell-free layer interface), and $dv_z/dr=0$ at $r=0$ (symmetry). We have numerically solved the above equation using finite differences and obtained the velocity profile that corresponds to the appropriate $U_{\max}$. The values of the pressure gradients (dP/dz) for various vessel sizes and H_D's are listed in Table III. This is the starting point for the problem. With a fully developed flow under a given pressure gradient, we will introduce the bubble and study the subsequent dynamics.

D. Bubble motion in the vessel

For this problem, the governing equations for the flow are given by Eqs. (1) and (2). The boundary and initial conditions for the problem in the presence of the bubble are as follows.

Inlet boundary, $z=0$. At the inlet, the fully developed two-fluid model axisymmetric Casson flow velocity profile and dP/dz are determined as above and are prescribed for the bubble problem.

Outlet boundary, $z=L$. Since the flow occurs in a long vessel, for computational purposes it is important to establish a geometry with a prescribed location for the outlet boundary. Here, the outlet boundary is set at $z=L=6d$. The rationale for $6d$ is explained later under Sec. V A. An outflow boundary condition at $z=L$ is prescribed as follows:

$$\frac{\partial \mathbf{u}}{\partial z}(r,L,t)=\mathbf{0}. \tag{14}$$

Reflective boundary, $r=0$. A reflective boundary condition is used at the axis of symmetry, $r=0$.

$$v_r(0,z,t)=0, \quad 0\leqslant z\leqslant L,$$

$$\frac{\partial v_z}{\partial r}(0,z,t)=0, \quad 0\leqslant z\leqslant L. \tag{15}$$

Wall no-slip boundary, $r=R$.

$$\mathbf{u}(R,z,t)=\mathbf{0}. \tag{16}$$

E. Initial conditions

At $t=0$, the flow is described by a fully developed velocity profile $(v_z(r))$ obtained by solving Eq. (13). Thus

$$\mathbf{u}(r,z,t=0)\rightarrow v_z(r)|_{t=0}. \tag{17}$$

F. Initial bubble shape and location

For $\lambda\geqslant 1$, the initial shape of the bubble is such that there is a thin annular fluid film between the bubble and the wall. The film thickness is set equal to $0.1R$. The initial shape may be either spherical $(\lambda<1)$ or a hemispherical capped cylindrical slug $(\lambda\geqslant 1)$ (for example, see Fig. 1). The subsequent shapes for $t>0$ are determined by the prevailing physics.

TABLE II. Centerline velocities for various vessel sizes (from [48]).

d (μm)	$U_{\max}$ (cm/s)
40 (small arteriole)	1.75
100 (large ateriole)	7.0
2000 (small artery)	35.0

TABLE III. Pressure gradient values for various H_D's and vessel sizes.

d (μm)	H_D	$\frac{dP}{dz}$ (dyn/cm^3)	$U_{\max}$ (cm s^{-1})
40	0.335	42500	1.75
40	0.4	50000	1.75
40	0.45	56500	1.75
100	0.335	31200	7.0
100	0.4	35000	7.0
100	0.45	41000	7.0
2000	0.335	427	35.0
2000	0.4	534	35.0
2000	0.45	645	35.0

TABLE IV. Reynolds number based on apparent viscosity μ_{app}, vessel diameter d, and U_{max} for various H_D's.

H_D	d (μm)	Re_{app}
0.335	40	0.36
0.335	100	2.9
0.335	2000	230.2
0.4	40	0.32
0.4	100	2.5
0.4	2000	183.2
0.45	40	0.29
0.45	100	2.15
0.45	2000	151.5

In physiological terms, our wall boundary may be taken to denote the endothelial surface layer (ESL) [49]. The bubble is positioned a diameter away from the inlet (bottom) boundary at the start of computations.

III. NONDIMENSIONALIZATION OF GOVERNING EQUATIONS

The governing equations are nondimensionalized using the following scheme: $\rho=\rho_l\rho^*$, $\mu=\mu_{ref}\mu^*$, $s=ds^*$, $r=dr^*$, $z=dz^*$, $\mathbf{u}=U_{max}\mathbf{u}^*$, $t=d/U_{max}t^*$, $p=\rho U_{max}^2/d$, $\gamma=U_{max}/d\gamma^*$, $\mathcal{K}=\mathcal{K}^*/d$, and $\hat{\delta}=(1/d^3)\hat{\delta}^*$. Here, the superscript * refers to nondimensional quantities, μ_{ref} is the reference viscosity, and U_{max} is the maximum inlet flow velocity. Here, μ_{ref} is taken to be an average blood viscosity (assumed to be equal to 3.5 cP). With these reference values, for vessel sizes of 40-μm-diameter small arteriole, 100-μm-diameter large arteriole, and 2000-μm-diameter small artery, the Reynolds numbers defined by $Re=\rho_l dU_{max}/\mu_{ref}$ are 0.2, 2, and 200, respectively. We compare these Reynolds number values with those derived on the basis of apparent viscosity μ_{app} given by Eq. (12). The latter Reynolds numbers are defined by $Re_{app}=\rho_l U_{max}d/\mu_{app}$. This comparison would enable us to discuss the results obtained in terms of Re's based on reference values and would avoid constant reference to particular parameters. The values of Re_{app} for three different H_D's and three vessel sizes are shown in Table IV. It is observed that the apparent Reynolds numbers are in the range of 0.2, 2, and 200. Thus, we will discuss the results of this paper in terms of these generic values.

For a vertical vessel configuration, Eqs. (1) and (2) become (after dropping the superscript *)

$$\nabla\cdot\mathbf{u}=0, \tag{18}$$

$$\frac{\partial\mathbf{u}}{\partial t}+\nabla\mathbf{u}\cdot\mathbf{u}=-\nabla p+\frac{1}{\mathrm{Re}}\nabla\cdot\mu(\nabla\mathbf{u}+\nabla^T\mathbf{u})+\frac{1}{\mathrm{We}}\int_{S(t)}\mathcal{K}\mathbf{n}_f\hat{\delta}(\mathbf{x}-\mathbf{x}_f)ds+\frac{1}{\mathrm{Fr}^2}\rho(-\mathbf{e}_z). \tag{19}$$

In Eq. (19), $\mathbf{e}_z$ is the unit vector along the axial direction.

The bulk viscosity expression given by Eqs. (6) and (8) in nondimensional form becomes

$$\mu_l=\begin{cases}\left[\dfrac{\mu_\infty}{\mu_{ref}}+\sqrt{\dfrac{\mathrm{Bi}}{|\gamma|}}(1-e^{-\sqrt{m|\gamma|}})\right]^2, & 0\leqslant r\leqslant(1-\delta)/2\\ \dfrac{\mu_{layer}}{\mu_{ref}}, & (1-\delta)/2<r\leqslant 0.5.\end{cases} \tag{20}$$

We note that there are four nondimensional parameters involved: the Reynolds number, Re, Weber number, We, Froude number, Fr, and Bingham number, Bi. The latter three are defined by

$$\mathrm{Bi}=\frac{\tau_y d}{\mu_{ref}U_{max}},\quad \mathrm{We}=\frac{\rho_l U_{max}^2 d}{\sigma},\quad \mathrm{Fr}=\frac{U_{max}}{\sqrt{gd}}.$$

Certain other parameters of interest may be obtained by a combination of the above numbers. For example, for $Re<1$, we consider the capillary number, $Ca=\mu U_{max}/\sigma=We/Re$ which is a ratio of viscous to surface tension forces. Three additional parameters that govern the problem are ρ_g/ρ_l, μ_g/μ_l, and λ.

IV. NUMERICAL METHOD

Equations (1) and (2) are solved subject to boundary conditions by Eqs. (13)–(16) and initial condition equation (17). The density and viscosity variations in Eqs. (1) and (2) are given by Eqs. (3), (4), (6), and (8).

The present study is based on a front-tracking method coupled with a level contour reconstruction procedure [6,7]. The key steps in the numerical algorithm are listed below.

(1) Given the interface position, calculate the surface tension forces and distribute them to the fixed Eulerian grid using a "density-weighted" distribution procedure.

(2) Smooth the jump in fluid properties across the interface using a smoothed-delta function.

(3) Solve the governing equations on the fixed Eulerian mesh using a projection method to obtain the divergence-free velocity and the pressure.

(4) Update the position of the interface by advecting in a Lagrangian fashion using the velocity field obtained in step (3).

(5) Reconstruct the interface using a level-contour reconstruction procedure if the bubble volume is less than 0.5% of the initial volume or after every few hundred time steps.

(6) Repeat steps (1)–(5) until steady state is reached or the bubble reaches the outlet.

These steps are briefly explained in the following.

A. Surface tension calculation

The surface tension force, $\mathbf{f}_{st}$, acting on a small segment of the interface surface is given by (see [7])

$$\mathbf{f}_{st}=\int_A^B\sigma\mathcal{K}\mathbf{n}_f ds=\sigma(\mathbf{t}_A-\mathbf{t}_B)-\mathbf{e}_r\sigma s_{AB}, \tag{21}$$

where $\mathbf{t}$ is the tangent vector on the interface, $\mathbf{e}_r$ is the unit radial vector, A,B are the end points of the interface seg-

ment, and s_{AB} is the length of the A-B segment. The calculated surface tension force on the marker points is then transferred to the fixed Eulerian cells using a numerical approximation of the $\hat{\delta}$ function appearing in Eq. (2). However, with such a distribution, interfacial numerical instabilities arise for flows involving high surface tension forces and large density and viscosity ratios. To avoid these instabilities, following [50], the surface tension force is distributed in a density-weighted manner as follows:

$$\mathbf{F}_{st(i,j)} = \frac{\sum_e \rho_{i,j}\mathbf{f}_{ste}D_{i,j}(\mathbf{x}-\mathbf{x}_m)}{\sum_e \rho_{i,j}D_{i,j}(\mathbf{x}-\mathbf{x}_m)}, \tag{22}$$

where $\mathbf{x}=(i\Delta r, j\Delta z)$, $\mathbf{x}_m=(r_m,z_m)$ is the midpoint of the interfacial segment e, $\rho_{i,j}$ is the density at the given Eulerian grid point (i,j), and $D_{i,j}$ is

$$D_{i,j}(\mathbf{x}-\mathbf{x}_m) = \frac{\hat{\delta}(r_m/\Delta r - i)\hat{\delta}(z_m/\Delta z - j)}{2\pi r \Delta r \Delta z}. \tag{23}$$

The one-dimensional delta function is numerically approximated as follows (see [51]):

$$\hat{\delta}(\hat{d}) = \begin{cases} \hat{\delta}_1(\hat{d}), & |\hat{d}| \leqslant 1 \\ 1/2 - \hat{\delta}_1(2-|\hat{d}|), & 1 < |\hat{d}| < 2 \\ 0, & |\hat{d}| \geqslant 2, \end{cases} \tag{24}$$

and $\hat{\delta}_1(\hat{d}) = (3-2|\hat{d}| + \sqrt{1+4|\hat{d}|-4\hat{d}^2})/8$. Here, $\hat{d}$ denotes the distance from the origin of the source (the front position). In an earlier paper [7], the equation for $\hat{\delta}(\hat{d})$ has a typographical error for the range $1<|\hat{d}|<2$. The factor $2-|\hat{d}|$ has to be properly introduced there.

From Eq. (24), it is evident that the support of the function $\hat{\delta}(\hat{d})$ is two cell widths on either side of the interface. Refining the grid by a factor of 2, therefore, halves the width of the $\hat{\delta}(\hat{d})$ function.

B. Smoothing of fluid properties

In the bubble dynamics problem, the ratios of the properties of the two fluids across the interface can be very large, for example, of the order of 1000 for density, and 100 for viscosity. Such sharp jumps complicate the simulation due to instabilities. To alleviate this, the discontinuities are smoothed out across a finite thickness proportional to the mesh size. This is achieved by a smoothed $\mathcal{H}(r,z,t)$ whose value varies from 1 in the continuous (bulk) phase to 0 in the dispersed phase. A smoothed solution for $\mathcal{H}(r,z,t)$ is found by solving a Poisson equation [52] as follows:

$$\nabla\cdot\nabla\mathcal{H}(r,z,t) = \nabla\cdot\int_{S(t)} \mathbf{n}_f\hat{\delta}(\mathbf{x}-\mathbf{x}_f)dS. \tag{25}$$

The sharp $\hat{\delta}$ distribution in Eq. (25) is written as a product of two one-dimensional delta functions along the radial and axial directions. Equation (25) is efficiently solved for the whole domain with appropriate boundary conditions using a multigrid method based on the red-black Gauss-Siedel (RBGS) smoother [53]. In our problem, a symmetry boundary condition $\partial\mathcal{H}/\partial r=0$ is used at $r=0$ and a Dirichlet boundary condition with $\mathcal{H}=1$ is used on all other boundaries. The density and viscosity are updated using

$$\rho(r,z,t) = \rho_l\mathcal{H}(r,z,t) + \rho_g[1-\mathcal{H}(r,z,t)], \tag{26}$$

$$\mu(r,z,t) = \mu_l\mathcal{H}(r,z,t) + \mu_g[1-\mathcal{H}(r,z,t)]. \tag{27}$$

C. Flow solver: Projection method

The conservation equations are discretized with a second-order finite difference based variable density projection method [34]. The velocity, density, and viscosity are all located at cell centers. The lagged pressure $p^{n-1/2}$ is located at cell corners with the superscript n denoting the time level. The time stepping procedure is based on the second-order Crank-Nicholson method.

Briefly, an intermediate velocity field is obtained using a semi-implicit viscous solves. The equation for the intermediate velocity $\mathbf{u}^*$ is given by

$$\rho^{n+(1/2)}\left(\frac{\mathbf{u}^*-\mathbf{u}^n}{\Delta t}\right) = -[(\mathbf{u}\cdot\nabla)\mathbf{u}]^{n+(1/2)} - G_p{}^{n-(1/2)} + \left(\frac{D^*+D^n}{2}\right) + \mathbf{F}_{st}^{n+(1/2)} + \rho^{n+(1/2)}\mathbf{g}, \tag{28}$$

where G_p, $D(\mathbf{u})=\nabla\cdot\mu^n(\nabla\mathbf{u}+\nabla^T\mathbf{u})$, and $\mathbf{F}_{st}$ represent the pressure gradient operator, the diffusion operator, and the discretized surface tension forces [see Eq. (22)], respectively. A second-order predictor-corrector method based on the unsplit Godunov method [54] is used to evaluate $[(\mathbf{u}\cdot\nabla)\mathbf{u}]^{n+(1/2)}$, and a standard second-order central finite difference is used for $D(\mathbf{u})$. For $D(\mathbf{u})$, the spatial distribution of viscosity is computed explicitly using the second invariant of the strain rate tensor evaluated at the nth time step. Thus, $\mu=\mu^n$ in Eq. (28) refers to the viscosity at the nth time step. Such an evaluation does not impose additional stability criterion as noted in [55]. The resulting equations for the velocity components of $\mathbf{u}^*$ [Eq. (28)] are solved by a multigrid method based on the red-black Gauss-Siedel (RBGS) smoother [53]. A projection method is invoked on $\mathbf{u}^*$ to obtain the divergence-free velocity $\mathbf{u}^{n+1}$. The projection step is given by the following equations:

$$\frac{\mathbf{u}^{n+1}-\mathbf{u}^n}{\Delta t} = \mathcal{P}\left(\frac{\mathbf{u}^*-\mathbf{u}^n}{\Delta t}\right),$$

$$\frac{1}{\rho^{n+(1/2)}}G_p{}^{n+(1/2)} = \frac{1}{\rho^{n+(1/2)}}G_p{}^{n-(1/2)} + (I-\mathcal{P})\left(\frac{\mathbf{u}^*-\mathbf{u}^n}{\Delta t}\right), \tag{29}$$

where $\mathcal{P}$ represents the discretization of the projection operator. The details of the steps involved in discretization of individual terms in Eqs. (28) and (29) for an axisymmetric case

and the corresponding time step restrictions for numerical stability are given in [34].

D. Interface advection

With the updated Eulerian velocity field, the front or marker points are advected in a Lagrangian fashion as follows:

$$\mathbf{x}_f^{n+(1/2)} = \mathbf{x}_f^n + \mathbf{V}^n \frac{\Delta t}{2}, \tag{30}$$

$$\mathbf{x}_f^{n+1} = \mathbf{x}_f^{n+(1/2)} + \mathbf{V}^{n+1} \frac{\Delta t}{2}, \tag{31}$$

where $\mathbf{V}$ is bilinearly interpolated from the fluid velocities, and $\mathbf{x}_f$ denotes the position of the front point. Adding Eqs. (30) and (31), we get

$$\mathbf{x}_f^{n+1} = \mathbf{x}_f^n + \left(\frac{\mathbf{V}^{n+1} + \mathbf{V}^n}{2} \right) \Delta t. \tag{32}$$

Thus, Eq. (32) guarantees a second-order accurate scheme for the advection equation of marker points.

E. Interface reconstruction and bubble volume conservation

In this study, both redistribution of the front points and conservation of the bubble volume are simultaneously enforced using a level contour reconstruction procedure [7,56,57]. With a significantly deforming interface, a new distribution of front points is needed. The $\mathcal{H}=0.5$ contour obtained by solving Eq. (25) represents the location of the interface and is reconstructed in each cell using a simple linear interpolation procedure (a point-slope calculation). The intersection points of these linear contour segments with the background Eulerian cells now form the new representation of the front. Also, the volume fractions of the bubble and the bulk fluids in each of the cells intersected by the contour segments can be directly computed, and the total volume of the bubble estimated. However, in some simulations, $\mathcal{H}=0.5$ contour may not always result in bubble volume conservation. For such cases, an optimum contour value, $\mathcal{H}_{\text{opt}}$, different from 0.5 is found through iterations such that a desired level of accuracy for the total bubble volume conservation (typically within 0.5% of the initial volume of the bubble) is achieved. The interface reconstruction is done every few hundred time steps or more depending on the circumstance or when the volume loss of the bubble exceeds 0.5% of the original volume. This serves as the criterion for interface reconstruction.

V. RESULTS AND DISCUSSION

A. Domain and grid sizes

Our problem entails solving for bubble motion in a long cylindrical vessel. For purposes of numerical computation, there is a need to define inlet and outlet numerical boundary locations which reflect the physics. Here, we estimate the optimal sizes of the numerical domain and of the grid for the computations.

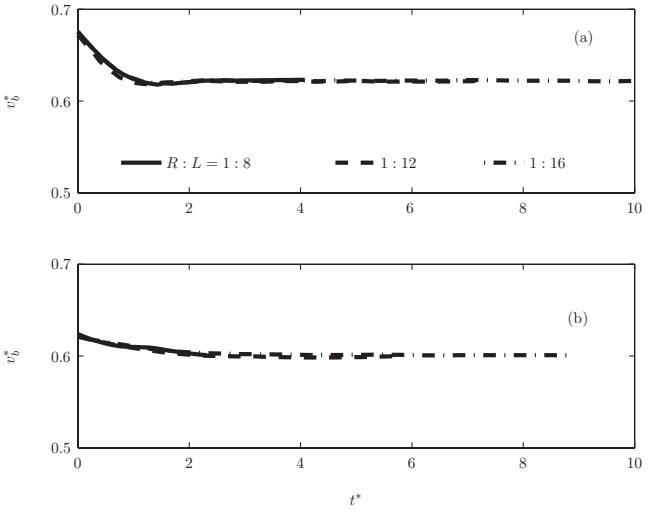

FIG. 4. Bubble velocity for Re=200 and (a) $\lambda=0.9$, and (b) $\lambda=1.3$, as a function of time for three aspect ratios ($R:L$).

Simulations are carried out for Re=200, $\lambda=0.9, 1.3$, and in a vertical configuration. Results are developed for three different domain sizes ($R:L$): 1:8, 1:12, and 1:16. We note that in order to assess an optimal size, it is enough to ascertain the size necessary for obtaining steady motion of both a bubble in a vertical vessel at the highest Re (buoyancy-assisted motion).

In Fig. 4, for identical conditions, the nondimensional velocity of the center of mass of the bubble, $v_b^*=v_b/U_{\max}$, is plotted as a function of nondimensional time t^*, for Re=200, $\lambda=0.9$ [Fig. 4(a)], and $\lambda=1.3$ [Fig. 4(b)]. For $\lambda=0.9$, it is noted that for all three sizes chosen, the bubble velocity asymptotes to a steady state value of ~ 0.62 at about $t^* \sim 2.5$. For $\lambda=1.3$, the bubble velocity asymptotes to a steady value of ~ 0.6 at about $t^* \sim 3$.

In Fig. 5, the steady state shapes of the bubbles corresponding to the cases of Fig. 4 are plotted at $t^*=2.6$ for $\lambda=0.9$ [Fig. 5(a)] and $t^*=3.1$ for $\lambda=1.3$ [Fig. 5(b)]. The vertical boundaries of the bounding boxes denote actual wall locations. The steady state shapes are noted to be identical. On the basis of these figures, we choose $R:L=1:12$ ($d:L=1:6$) for all of our subsequent calculations. With a smaller $R:L$, the bubble would exit the domain before attaining the steady state, while a larger $R:L$ is not computationally efficient.

The effect of grid size on the solutions are next investigated. Uniform grid spacings along both radial and axial directions are used. Our intention is to determine the optimal grid size to accurately evaluate the near-wall events. Two grid sizes ($N_r \times N_z$), where N_r and N_z are the number of grid points along the radial and axial directions, are considered: a 64×768 grid and a twice finer 128×1536 grid. As noted earlier, for the 128×1536 grid, the interface thickness is halved compared to the 64×768 grid. With each grid size, simulations are done for two cases, Re=0.2, $\lambda=1.0$ and Re=200, $\lambda=1.3$. The steady state bubble shapes for these cases are shown in Fig. 6 for both grid sizes. For both grid sizes,

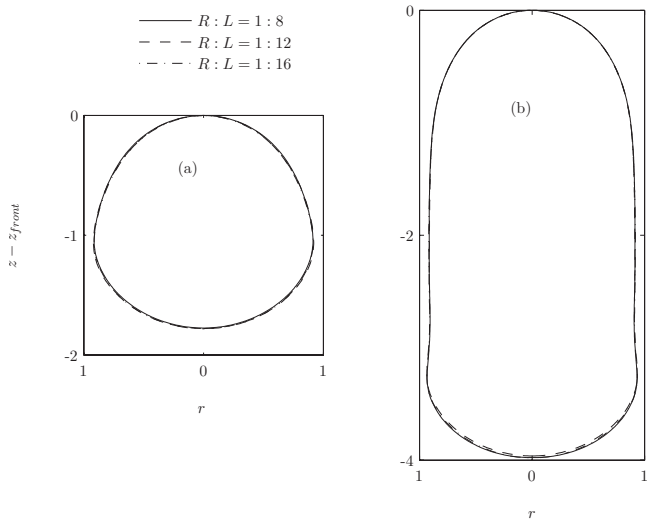

FIG. 5. Steady state bubble shapes for Re=200 and (a) $\lambda=0.9$, and (b) $\lambda=1.3$, for three aspect ratios. z_{front} denotes the axial location of the bubble's front stagnation point.

the steady state shapes and the annular fluid film thicknesses are the same. The corresponding streamlines in and around the bubble are also identical (not displayed here). Thus, a 64×768 grid is noted to be sufficiently accurate.

B. Validation of the numerical scheme

Results appropriate for a bubble motion in Casson fluid through a circular vessel are not available at the present time to enable a straightforward validation. Predictions for the steady state dynamics are compared with the experimental results of Ho and Leal [18], and the numerical evaluations of Martinez and Udell [17]. Ho and Leal [18] have presented results for the drop velocity, drop shape, pressure drop, and streamlines for the creeping motion of neutrally buoyant Newtonian drops ($\rho_g/\rho_l=1$) through a circular vessel. The

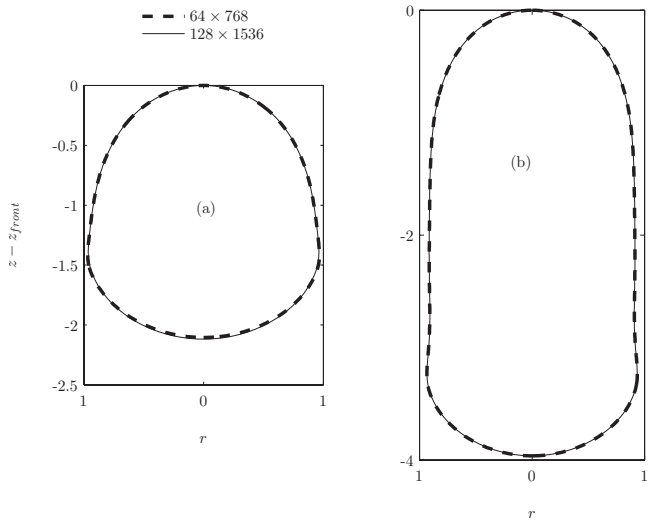

FIG. 6. Steady state bubble shapes for (a) Re=0.2, $\lambda=1.0$, and (b) Re=200, $\lambda=1.3$ with $R:L=1:12$ and two grid sizes 64×768, 128×1536.

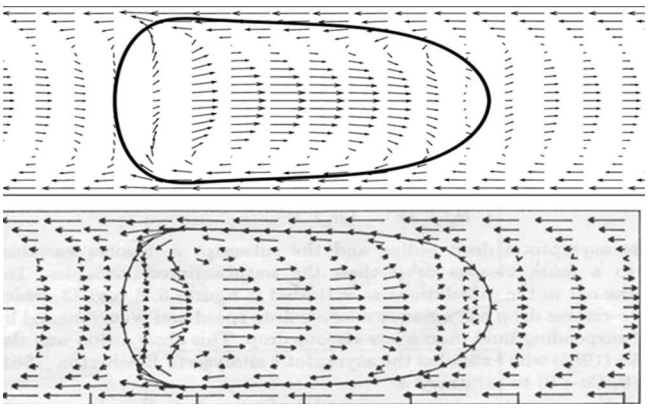

FIG. 7. Comparison of the present numerical solution (top) with the boundary element solution [Fig. 3(b) in [17]] (bottom).

drop diameter is comparable to the diameter of the vessel. For the case where $\mu_g/\mu_l=0.19$, Ca=0.1, and Re=0.06, the dimensionless steady state velocity of the drop (based on mean inlet velocity) is measured to be ~1.39 and this compares with our numerical prediction of 1.39. Martinez and Udell [17] have employed a boundary element technique for solving a similar problem with Re set to zero, and predict this velocity to be 1.45. Comparisons of our flow field predictions with those of Martinez and Udell [17] are displayed in Fig. 7 and are noted to be qualitatively very similar.

Next, we compare our results for the rise of a Newtonian fluid drop in a shear thinning fluid medium with the numerical results of Ohta *et al.* [16] for identical conditions and an identical rheological model. They have used a volume of fluid method. The shear thinning fluid is modeled by a four parameter Carreau-Yasuda fluid (sodium acrylate polymer—SAP). The dimensional values of parameters for the case are $\rho_l=1.0014$ gm/cm^3, $\rho_g=0.971$ gm/cm^3, and initial drop diameter equal to 0.914 cm. Following [16], the variation of the bulk liquid viscosity is given below.

$$\mu_l=\frac{\mu_0}{[1+\mu_0/\tau^*|\dot{\gamma}|^a]^{(1-n)/a}},\quad \text{for } |\dot{\gamma}|<A, \tag{33}$$

$$\mu_l=\hat{\mu}_{\text{SAP}\infty},\quad |\dot{\gamma}|\geqslant A, \tag{34}$$

where a, n, τ^* are model parameters, $|\dot{\gamma}|$ is the shear rate as given by Eq. (9), and μ_0 and $\hat{\mu}_{\text{SAP}\infty}$ are the asymptotic viscosities at zero and infinite shear rates, respectively. Also, $A=100$ s^{-1}, is the experimentally obtained shear rate at the intersecting point of the Carreau-Yasuda model and $\hat{\mu}_{\text{SAP}\infty}$. The values of various other parameters are given in Table V.

The steady state Reynolds number predicted by our scheme is 37 and this compares with 35 given by Ohta *et al.*

TABLE V. Values for parameters given in Eqs. (33) and (34) for the highly shear-thinning SAP liquid.

μ_0 (Pa s)	τ^* (Pa)	n	a	$\hat{\mu}_{\text{SAP}\infty}$	A (s^{-1})
0.026	0.018	0.4	4.0	0.0013	100

TABLE VI. Estimated values of nondimensional parameters. Values of μ_{ref}=3.5 cP, ρ_{ref}=1.0 gm/cm^3, and σ=50 dyn/cm are assumed.

d (μm)	U_{max} (cm s^{-1})	Re	Ca	We	Fr
40	1.75	0.2	1.225×10^{-3}	2.45×10^{-4}	0.88
100	7.0	2	4.9×10^{-3}	9.8×10^{-3}	2.24
2000	35.0	200	2.45×10^{-2}	4.9	2.5

[16]. These experimental and numerical validations of our procedure lend credibility to our results.

C. Detailed study of the motion of occluding bubbles under various conditions

In this section, we describe the motion of an occluding bubble in three different vessel sizes. The vessel sizes are representative of a small artery (d=0.2 cm), a large arteriole (d=100 μm), and a small arteriole (d=40 μm) in a normal human. The values of various parameters used in the simulations are given in Table VI. The simulations are done for both horizontal and vertical vessels. As stated earlier, for arteriolar vessels of 40 and 100 micron sizes, a distinct cell-free layer is considered that occurs due to a net lateral migration of the particles away from the vessel wall (see [47]). In the calculations, σ is taken as 3 dyn/cm (Ca=2×10^{-2}) for Re=0.2, and 10 dyn/cm for Re=2 (Ca=2.45×10^{-2}) although the air-blood surface tension coefficient may be around σ=50 dyn/cm. The reduced value chosen for σ is necessitated by the fact that for low Re and very high σ ($\Rightarrow$ low Ca), spurious parasitic currents appear near the interface. Such spurious currents have been reported in other studies for similar circumstances [52]. An artificial reduction in the value of σ is not required at higher values of Re. The impact of the choices for σ is discussed elsewhere in the text.

A short duration after bubble release in the fully developed flow, the bubble velocity and shape attain steady states. During its motion, the bubble experiences the following: (a) inertia force due to applied pressure gradient, (b) viscous and wall forces, (c) surface tension forces, and (d) gravity.

In Fig. 8, the steady state bubble shapes at Re=0.2, 2, and 200 for λ=0.9, 1, and 1.05 are displayed. The hematocrit value H_D is set equal to 0.45. In the plots, the front stagnation point of the steadily moving bubble is taken as the origin and a scale length is identified on the ordinate. This is done to display the extent of deformation. From Table VI, it is evident that at Re=0.2 and 2, capillary effects dominate both inertial and viscous effects (Ca, We$\ll$1), and for λ=0.9 the bubbles remain nearly spherical. At these Re's, for $\lambda\geq1$, bubbles nearly occlude the vessels. The shapes predicted for Re=0.2 are qualitatively consistent with both the experimental observations of Ho and Leal [18] and the numerical results of Martinez and Udell [17]. For Re=200, inertial forces dominate capillary and viscous forces (We$\sim$5 and Ca$\ll$1). For λ=0.9, the interface deformation due to the inertia of the bulk fluid is most pronounced at the trailing end resulting in a flatter interface. The bubble is prolate spheroidal at the front. For $\lambda\geqslant1$, the bubble deforms appreciably in the axial direction because of high interface stretching due to fluid inertia and increased wall effects.

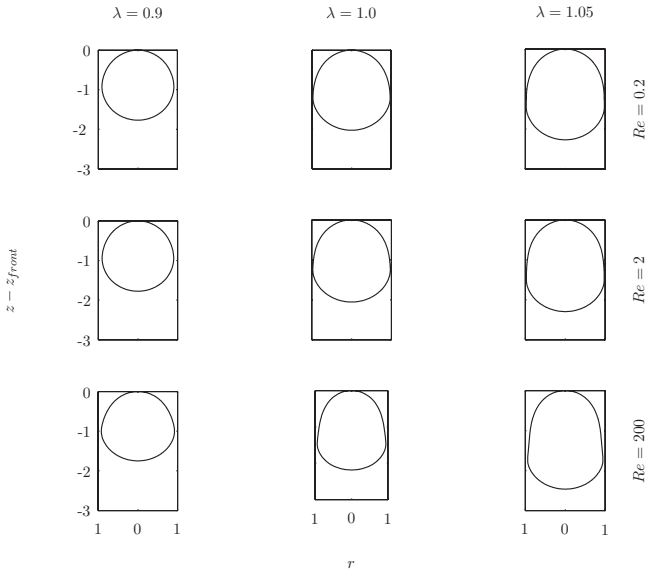

FIG. 8. Plot of steady state bubble shapes for Re=0.2, 2, and 200 and λ=0.9, 1.0, and 1.05.

To quantitatively assess the extent of deformation, the following deformation parameters are introduced after the bubble attains its steady shape: the axial length of the bubble, $\zeta=L_{axial}/2R$, the maximum radial extent of the bubble $\xi=L_{radial}/R$, and the ratio $\eta=\zeta/\xi$. These are plotted in Figs. 9(a)–9(c), respectively.

Consider the cases for Re=0.2 and 2. From Fig. 9(a), ξ linearly increases with λ up to 0.95. In the range $0.9\leqslant\lambda\leqslant0.95$, the bubble is nearly spherical due to the dominance of surface tension forces (see Table VI). The weak deviation from sphericity is due to the applied pressure gradient. This deviation is lesser for Re=2 compared to that for 0.2 because of the increased role of the wall effect as Re increases. The wall effect is such as to resist increased radial deformation

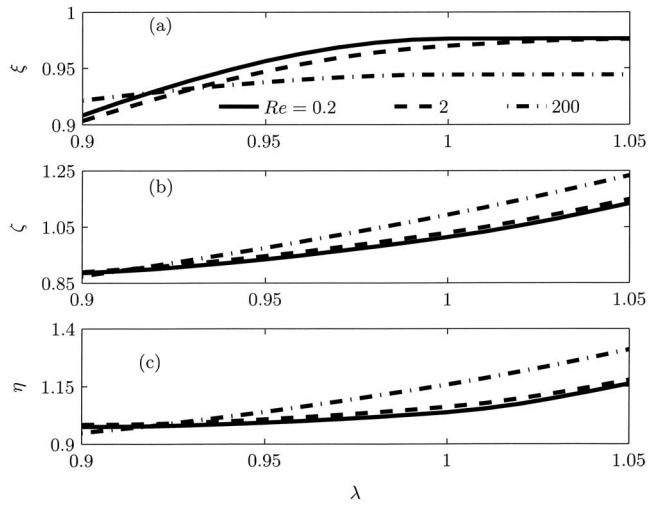

FIG. 9. Calculated bubble deformation factors for different Re's as a function of λ.

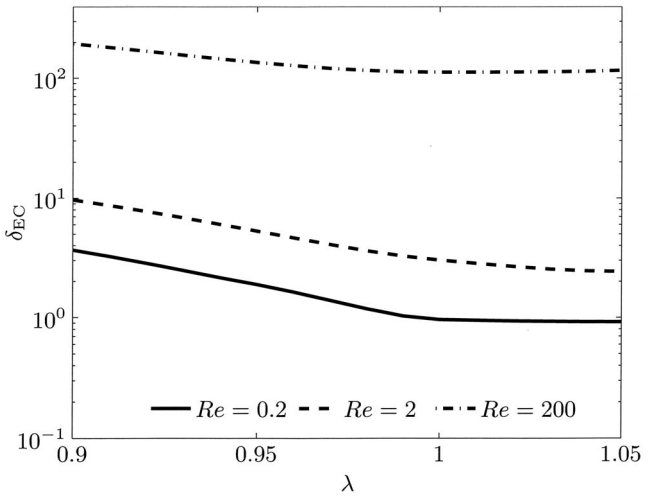

FIG. 10. Minimum film thickness normalized with L_{ESL}, as a function of λ for various Re's.

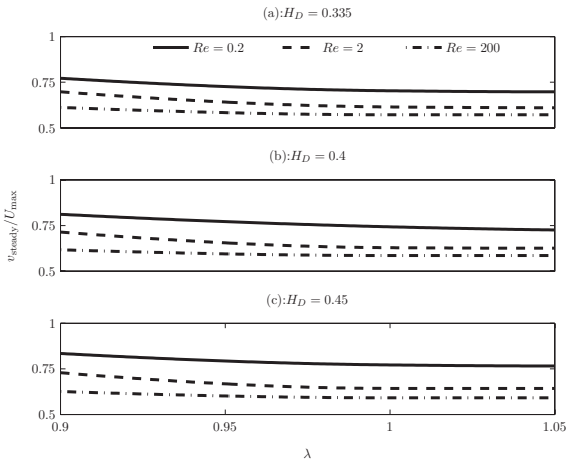

FIG. 11. Bubble steady state velocities for different Re's and H_D's as a function of λ. (a) H_D=0.335, (b) H_D=0.4, and (c) H_D =0.45. Curve legends for (b) and (c) are the same as (a).

that is favored by the applied pressure gradient. Beyond λ =0.95, there is significant competition between wall-induced forces and capillary effects. The rate of change of ξ decreases with increasing λ up to λ=1. For $\lambda > 1$, the deformation is negligible and ξ asymptotes to around 0.98. We now assess the loss of accuracy incurred by employing σ =3 dyn/cm and 10 dyn/cm for Re=0.2 and 2, respectively. For Re=0.2, the asymptotic value of ξ may be estimated following Bretherton [58]. Bretherton [58] has studied the motion of a semi-infinite bubble in a Newtonian pipe flow and has demonstrated that the film thickness is proportional to $Ca^{2/3}$. For fixed μ_{ref} and U_{max}, the film thickness is therefore $\propto\sigma^{-2/3}$ and this leads to ξ to be $\approx$0.997 with σ =50 dyn/cm. Although we are dealing with a finite-sized bubble, such an estimate is useful. For Re=2 and low Ca, based on the study of Heil [59] and Giavedoni and Saita [60] for a semi-infinite bubble at finite Reynolds numbers, ξ $\approx$0.993 and this compares with 0.98 obtained here.

The variation of ζ as a function of λ is displayed in Fig. 9(b). For λ up to 0.95, an increase in ζ is commensurate with the increase of ξ because of near sphericity of the bubbles in this regime. For $0.95 \leqslant \lambda < 1$, the rate of increase of ζ is higher due to increased wall effects. It may be noted that the bubble deformation is unconstrained in the axial direction. For $\lambda \geqslant 1$, the deformation is essentially axial. If we now approximate the shape of the bubble by a hemispherical capped cylinder (see Fig. 8), based on bubble volume conservation, it may be shown that $\zeta \propto \lambda^3$ in this regime. From Fig. 9(c), it is evident that for $0.9 \leqslant \lambda < 0.95$, η is near unity and the bubble is essentially spherical.

Next, we consider Re=200 in Figs. 9(a)–9(c). For λ =0.9, there is considerable bulging at the rear of the drop due to fluid inertia (We$\sim$5) causing ξ to be higher than λ [see Figs. 9(a) and 9(c)]. With increasing λ up to 0.96, ζ increases at a higher rate than ξ. This is attributable to the combined effects of the wall and fluid inertia. Beyond λ=0.96, the radial deformation is negligible and extension is purely axial with a λ^3 dependence [see Fig. 9(b)].

In Fig. 10, the dimensionless film thickness δ_{EC} $=(R-L_{radial})/L_{ESL}$ is plotted as a function of λ for various Re's. Here, L_{ESL} is the thickness of an endothelial surface layer (ESL) and is assumed to be $\sim$0.5 μm (see [49]). The ESL is an extracellular layer of cell membrane-bound substances that is actively involved in many functions, such as the control and regulation of vascular tone, fluid and solute exchange, haemostasis, and coagulation and inflammatory responses [49]. The ESL restricts the flow of plasma and can exclude red blood cells and some macromolecular solutes. Hence, L_{ESL} is a scale along the crosswise direction (perpendicular to the flow) and is useful for estimating the proximity of the bubble surface to the cell layer. The thickness δ_{EC} is therefore, a measure of the proximity of the bubble interface to the endothelial cell (EC) surface—an important parameter in the study of gas embolism. It is known that a closeness between the gas bubble surface and the EC surface is responsible for the initiation of cellular responses such as intracellular calcium (Ca^{2+}) signaling. In the problem studied, δ_{EC} is smallest for Re=0.2 and is higher for Re=2 and 200. In fact, for Re=0.2 and 2, and $\lambda > 1$, $\delta_{EC} \sim O(1)$, and the minimum film thickness ($R-L_{radial}$) is of the same order as L_{ESL}, while for Re=200 and all λ's, the bubble surface could be as far away as 100 L_{ESL}. Thus, for steady arteriolar flows corresponding to Re=0.2 and 2, the bubble surface is essentially in direct contact with the EC surface compared to flows in larger arteries. This can lead to larger endothelial cell deformations and potentially determine the fate of the endothelial cells lining the vessel wall.

In Figs. 11(a)–11(c), the variations of dimensionless steady state bubble velocities, v_{steady}/U_{max} for various Re's are plotted as a function of λ and H_D. At a fixed Re, for $0.9 < \lambda < 1$, v_{steady} decreases. This is due to both increased occlusion with increase in size and increase in form drag because of shape deformation. However, until λ=0.95, the deformation is very small (see Figs. 8 and 9) and the velocity decrease is due entirely to increased size. For $1 \leqslant \lambda \leqslant 1.05$, the reduction in velocity is very small because the deformation is largely a result of axial extension of the bubble and thus the bubble cross section remains essentially independent of λ [18] (see also Fig. 8).

The steady state flow fields and the wall shear stresses will now be discussed both in an inertial frame and in a

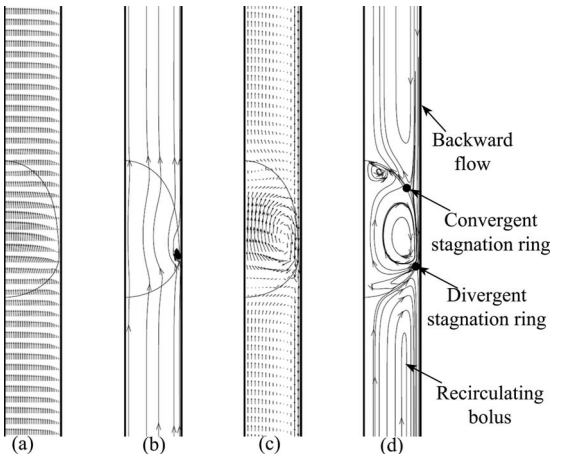

FIG. 12. Re=0.2, λ=1.05: Velocity vectors and streamlines as observed in [(a) and (b)] an inertial frame, and [(c) and (d)] a frame moving with the steady state velocity of the bubble.

reference frame attached to the center of mass of the bubble (moving frame). The steady state bubble velocities are such that there exists a region near the vessel axis that moves faster than the bubble. In the following, we restrict consideration to Re=0.2 with λ=1.05 (see Fig. 12). This is the only case that will be considered since the flow field behaviors are qualitatively similar for all the other cases. In Figs. 12(a) and 12(b), the velocity vectors and streamlines are plotted as viewed in an inertial frame while in 12(c) and 12(d) they are in the moving frame. The surface mobility of the bubble gives rise to a Hill's vortex which largely fills the volume of the bubble accompanied by two weaker secondary internal vortices, one near the front and the other near the rear stagnation points [see Figs. 12(c) and 12(d)]. The sense of rotation of the secondary vortices is opposite to that of the primary vortex and the corresponding shear stresses will have opposite signs. Two distinct bolus formations may be discerned, one at the front and one at the rear. Two stagnation rings (convergent and divergent) appear on the bubble surface at the points of intersection of the backward flow near the wall and the recirculating boluses [see Fig. 12(d)]. With increasing Re, the strengths of the secondary internal vortices increase (not shown here). The recirculating vortex seen in the streamline plot of Fig. 12(b) is due to entrainment of the fluid as it moves past the wall. This flow feature has significant effects on the distribution of the shear stress and its gradients (both temporal and spatial) at the cell surfaces. This will be discussed in detail in a later section.

A quantity of interest is the time variation of shear stress τ at any given point on the vessel wall due to the movement of the bubble. This point may in fact be located on the surface of an EC that lines the vessel wall; wall shear stress, $\tau=-\mu_l(\partial v_z/\partial r)$. Let τ_{ref} denote the basal shear stress which is the value of the wall shear stress under fully developed flow conditions in the absence of the bubble. Then, $\tau-\tau_{\text{ref}}$ denotes the "shear stress excess" experienced by the endothelial cell. The values of τ_{ref} are listed for various Re's in Table. VII.

Variations of shear stress excess normalized with τ_{ref} as a function of dimensionless time t^*, are displayed in Fig. 13 for Re=0.2, 2, and 200 with λ=1.0 and H_D=0.45. Although

TABLE VII. Basal shear stress (τ_{ref}) values for various Re's at H_D=0.45.

d (μm)	Re	Basal shear stress, τ_{ref} (dyn/cm^2)
40	0.2	56
100	2.0	104
2000	200	32.4

the magnitudes of shear stress excesses may differ, the variations are qualitatively similar in view of the similarities in the steady state flow features. We now consider a representative case such as illustrated in Fig. 13(b) corresponding to Re=2 and λ=1. The time variation of the shear stress excess

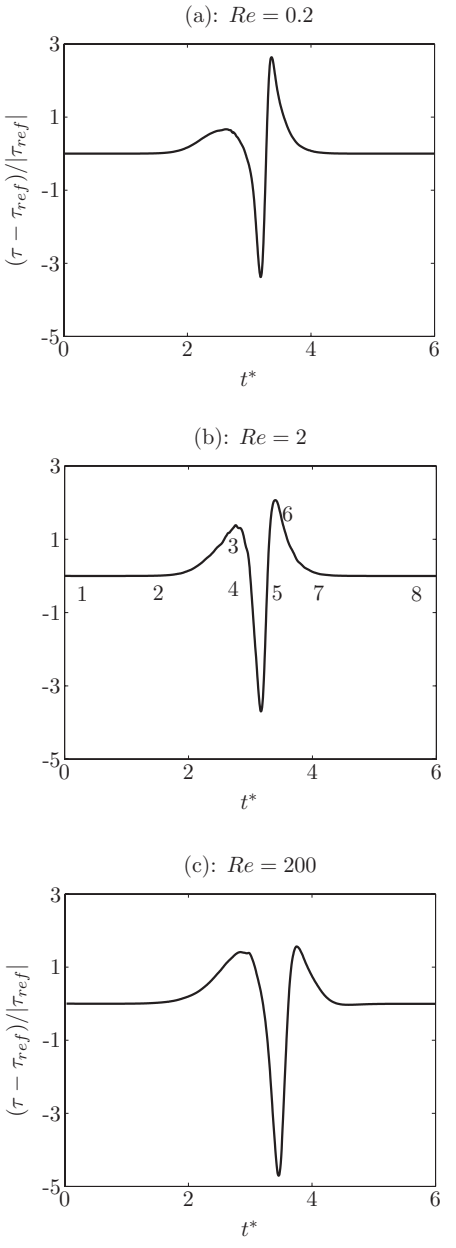

FIG. 13. Shear stress excess as a function of time for a given location on the endothelial cell surface lining the vessel wall for Re=0.2, 2, and 200 with λ=1.0.

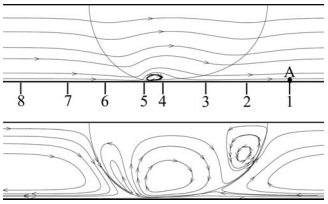

FIG. 14. Steady state flow field for Re=2 and λ=1.0 as viewed in an inertial frame (top) and in a reference frame attached to the moving bubble (bottom). Numbers 1–8 correspond to dimensionless times 1–8 in Fig. 13(b).

may be regarded as a solitary axial wave that traverses across all points on the "endothelial cell" lined vessel surface (lumen). The wave speed is equal to v_{steady}. The solitary wave at a typical point on the surface of an endothelial cell is depicted in Fig. 13(b). This point is denoted by "*A*" in Fig. 14, which shows steady state flow fields as viewed in both inertial and moving frames. Numbers 1–8 in Fig. 13(b) correspond to spatial locations 1–8 in Fig. 14. These numbers 1–8 in succession describe circumstances at *A* as the bubble approaches, traverses, and passes by this point. During stage 1–2, the bubble has a negligible effect at *A*. The pressure gradient at *A* is nearly constant and the shear stress remains at the basal value. During stage 2–3, local fluid velocity near *A* is increased. Both the pressure gradient and the flow rate at *A* are higher than the basal values and there is a corresponding increase in the shear stress. During stage 3–4, the flow decelerates and the shear stress gradually reduces to zero at 4. The pressure gradient reverses from being favorable to adverse during this time. When *A* is located between 4 and 5, flow reversal occurs due to the recirculating vortex (see Fig. 14), forming a shear stress regime of particular interest. This effect arises due to the finite size of the bubble and the resultant physical interplay of the trailing gas-liquid interface, the bulk liquid, and the presence of the wall. The shear stress switches direction becoming negative. During 5–6, there is fluid entrainment and a local increase in fluid velocity along the direction of motion of the bubble. This causes the shear stress to abruptly become positive, with its maximum value reached at point 6. The magnitude of shear stress at 6 is higher compared to that at 3. During stage 6–7, the entrainment effects become weaker and the shear stress gradually returns to the basal value. Beyond 7, the bubble has effectively passed by and no longer has any tangible influence on the wall shear stress. During 7–8, the shear stress remains at its basal value.

The solitary wave creates both temporal and spatial shear stress gradients at the cell surface. These gradients coupled with sign reversals result in both compression (negative shear) and stretch (increased tension due to positive shear excess) of the cell membrane. For all Re's considered, the spatial variation in shear stress excess is noted to occur over the axial length of the bubble (L_{axial}) (see Fig. 14), and thus is a function of λ and Re [see Fig. 9(b)]. Now, let L_{EC} denote the length of the endothelial cell along the streamwise direction. This is ≈140 μm under physiological flow conditions [61]. The ratio $L_{\text{axial}}/L_{\text{EC}}$ provides an estimate of the spatial variation of the shear stress along the surface of the cell.

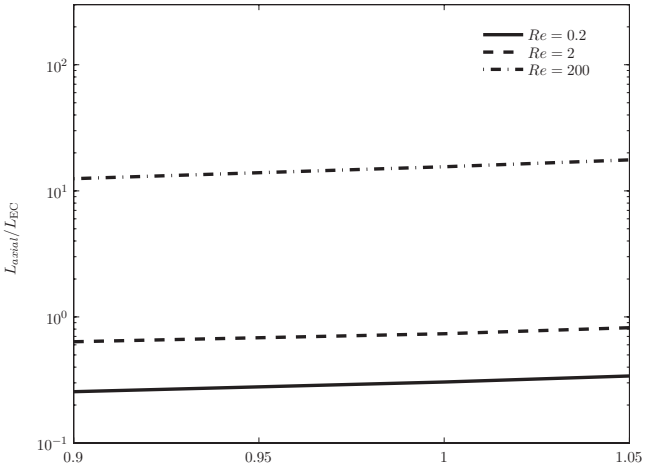

FIG. 15. Bubble axial length normalized with endothelial cell width as a function of λ.

These values are given in Fig. 15 as a function of λ for various Re's. Consider the particular circumstance when the bubble is situated directly over a typical endothelial cell such that the centers of the bubble and the cell surface are aligned along the same radial line. For Re=0.2 and 2, $L_{\text{axial}}/L_{\text{EC}} < 1$ and the bubble covers just a fraction of the endothelial cell surface. For Re=200, $L_{\text{axial}}/L_{\text{EC}} > 10$ and the bubble covers many endothelial cell surfaces. Therefore, for Re =0.2 and 2, the shear stress excess varies over a portion of the endothelial cell surface, while for Re=200, this spatial variation may be spread over a large number of neighboring endothelial cells. The spatial variation of shear stress is pronounced for flows in arterioles.

The major potential physiologic implications of the shear stress solitary wave progression across the cell surface are the induction of endothelial cell membrane stretch [62], activation of mechanotransduction pathways [63,64], loss of plasma membrane integrity [65], and plasma membrane stress failure [62,66]. Studies of cell membrane mechanics and mechanotransduction typically feature homogeneous (i.e., whole cell) mechanical stress exposures without spatial gradients being exerted across the cell surface (see [64]). In experiments in which the influence of changes in shear stress are examined, cell membrane mechanics are spatially heterogeneous, reflecting the spatial heterogeneity of the shear stress exposure [63]. In such experiments, the rate of change of the shear stress exposure is either extremely slow (on the order of 20 dyn/cm^2 per min) or the magnitude of the step change in shear stress is relatively small [63]. Our results demonstrating the appearance of the shear stress solitary wave are both temporally and spatially different from anything that has been specifically studied experimentally [64]. The time rate of change of the shear stress during both the descent to the absolute minimum value and the subsequent rise to the absolute maximum value depicted in Fig. 13 are such that the point location on the cell surface is subjected first to a compressive impulse followed immediately by a tensile impulse. The spatial shear stress gradients, their impulsive nature, and the cell deformation they invoke may be the cause of alterations of vascular reactivity, endothelial cellular injury, and cell loss previously reported [67,68]. This

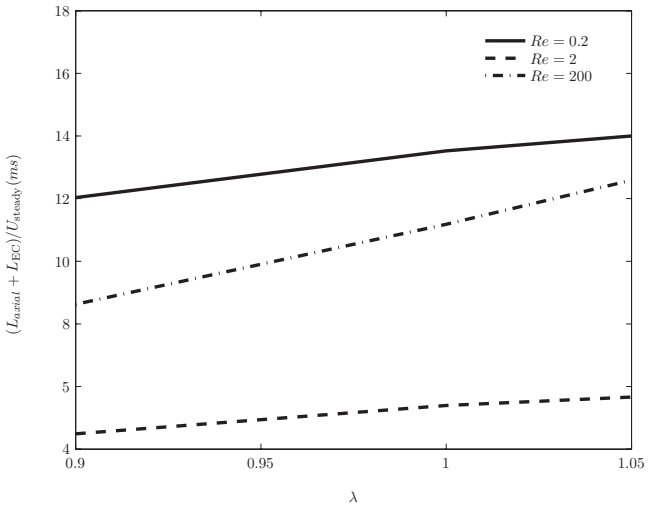

FIG. 16. Dimensional bubble residence times (milliseconds) for various Re's as a function of λ.

can happen through mechanisms involving stress failure of the lipid bilayer, overload influx of calcium ions stimulated by mechanosensing, alterations induced in cell cytoskeletal elements, and pathways involving changes in focal adhesion sites [64].

We next discuss the "bubble residence time." The residence time is defined as the time taken by the axial length of the bubble to pass over an endothelial cell. At steady state, the bubble residence time is then given by $(L_{\text{axial}}+L_{\text{EC}})/v_{\text{steady}}$. and is plotted in Fig. 16 for H_D=0.45. For illustration, at Re=0.2, 2, and 200 and λ=0.9, the v_{steady} values are ~1.5, 5.0, and 22.0 cm/s, respectively, and the corresponding steady state L_{axial} values for the bubble are ~36, 89, and 1750 μm. With L_{EC}~140 μm, the residence times are 0.012, 0.005, and 0.009 seconds, respectively. The residence time for Re=0.2 is noted to be the highest. Furthermore, at Re=0.2, the bubble interface is closest to the cell surface (see Fig. 10) and the shear stress spatial gradient is the largest (see discussions in Fig. 15). The cell damage may be most pronounced in this case. For the case of Re=2, the residence time is less than that for Re=200 by almost a factor of 2. For Re=2, the bubble interface is very close to the cell surface (see Fig. 10) compared to that at Re=200. The shear stress spatial gradient is more pronounced for Re=2 compared to Re=200 (see discussions in Fig. 15). In view of these, although the residence time for Re=2 is lesser compared to that at Re=200, the cell damage may still be severe at Re=2. This is consistent with prior observations that vascular responses, including vessel wall reactivity during arterial gas embolism are most pronounced with slow bubble motion (lower Re) slightly in advance of the cessation of blood flow [4,67,69,70].

D. Flow through horizontal vessels: A comparison

We now compare the results of the vertical vessel configuration with that of the horizontal. For a given pressure drop and vessel size, the effects of buoyancy are highest for the smallest sized bubbles (i.e., for λ=0.9). We shall consider two representative cases viz., Re=0.2, λ=0.9, and Re=200, λ=0.9, both with H_D=0.45. In Figs. 17 and 18, the steady state bubble shapes and the time evolution of the bubble velocities towards steady states for both the vessel configurations are displayed. The results are identical. Such identical results have also been obtained for H_D=0.335 and 0.4 (results not shown). From Table VII, for Re=0.2, Fr~0.9, and for Re=200, Fr~2.5. These imply that even for a free stream bubble motion (in the absence of confining walls), fluid inertia is of the same order as gravity along the axial direction. In the presence of the confining wall and high physiological flow rates (and pressure drop) such as in our study, the effects of gravity in determining the bubble dynamics are substantially diminished. For nearly occluding bubbles, axisymmetry holds and the gravitational effects are negligible along the radial direction. For flows in arterioles and small arteries, under normal physiological conditions, the effects of gravity may not be important. This result is consistent with the experimental results of Souders *et al.* [2] who observed that flow effects dominate bubble motion in smaller vessels.

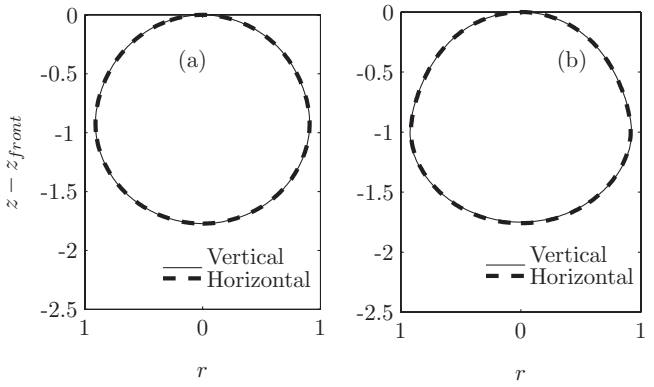

FIG. 17. Comparison of steady state bubble shapes for horizontal and vertical vessel configurations for (a) Re=0.2, λ=0.9, and (b) Re=200, λ=0.9.

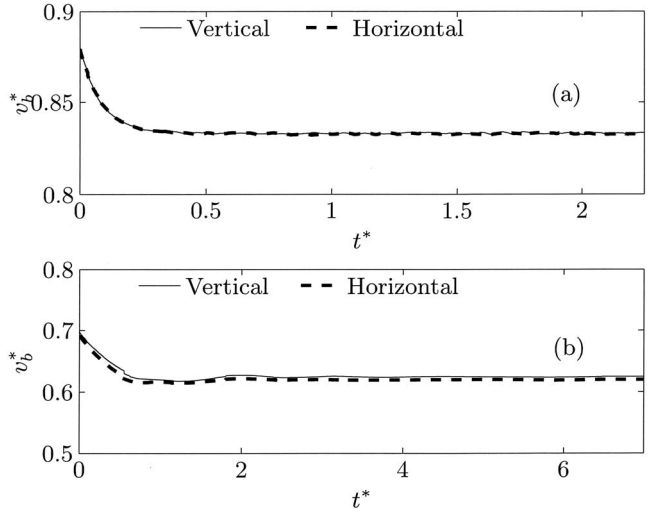

FIG. 18. Comparison of evolution of bubble velocities for horizontal and vertical vessel configurations for (a) Re=0.2, λ=0.9, and (b) Re=200, λ=0.9.

VI. CONCLUSIONS

A rigorous mathematical formulation has been developed and numerically solved for the axisymmetric motion of a finite-sized gas bubble moving in a blood vessel. Our simulations may serve as benchmark results for problems related to vascular bubble dynamics. The important physical insights gained from the numerical computations are as follows:

(1) At steady state, for all λ's, the bubble interface is closest to the endothelial cell surface in small arterioles (Re=0.2). This distance is higher in large arterioles (Re=2) and more so in small arteries (Re=200).

(2) For a finite-sized bubble, a recirculation vortex appears near its trailing meniscus. This creates both large temporal and spatial gradients of shear stress on the endothelial-cell lined vessel wall as the bubble approaches, moves over, and passes it by. Such spatial gradients are significantly higher on endothelial cells in arterioles than in small arteries.

(3) For the parameters examined, the bubble residence time is the highest in a small arteriole (Re=0.2). This is followed by that for a small artery (Re=200), and is the smallest for the large arteriole (Re=2).

(4) For occluding bubble motion in small arteries and arterioles, the role of gravity is negligible. This is consistent with experimental observations.

ACKNOWLEDGMENTS

We gratefully acknowledge NIH Grant No. R01 HL067986, NASA Grant No. NNX07AP97G, and ONR Grant No. N00014-08-1-0436 for supporting this study.

[1] J. L. Bull, Crit. Rev. Biomed. Eng. **33**, 299 (2005).
[2] J. E. Souders, J. B. Doshier, N. L. Polissar, and M. P. Hlastala, J. Appl. Physiol. **87**, 1937 (1999).
[3] D. P. Cavanagh and D. M. Eckmann, J. Fluid Mech. **398**, 225 (1999).
[4] D. M. Eckmann and V. N. Lomivorotov, J. Appl. Physiol. **94**, 860 (2003).
[5] A. Suzuki and D. M. Eckmann, Anesthesiology **99**, 400 (2003).
[6] J. Zhang, D. M. Eckmann, and P. S. Ayyaswamy, J. Comput. Phys. **214**, 366 (2006).
[7] K. Mukundakrishnan, S. Quan, D. M. Eckmann, and P. S. Ayyaswamy, Phys. Rev. E **76**, 036308 (2007).
[8] K. Mukundakrishnan, D. M. Eckmann, and P. S. Ayyaswamy, Ann. N.Y. Acad. Sci. (to be published).
[9] A. S. Popel and P. C. Johnson, Annu. Rev. Fluid Mech. **37**, 43 (2005).
[10] D. Rodrigue, D. De Kee, C. F. Chan Man Fong, and J. Yao, J. Non-Newtonian Fluid Mech. **86**, 211 (1999).
[11] D. Rodrigue, AIChE J. **47**, 39 (2001).
[12] D. Rodrigue, Can. J. Chem. Eng. **80**, 289 (2002).
[13] W. A. Hyman and R. Skalak, AIChE J. **18**, 149 (1972).
[14] T. Tsukada, H. Mikama, M. Hozawa, and N. Imaishi, J. Chem. Eng. Jpn. **23**, 192 (1990).
[15] O. Mitsuhiro, E. Iwasaki, E. Obata, and Y. Yoshida, J. Non-Newtonian Fluid Mech. **116**, 95 (2003).
[16] O. Mitsuhiro, E. Iwasaki, E. Obata, and Y. Yoshida, J. Non-Newtonian Fluid Mech. **132**, 100 (2005).
[17] M. J. Martinez and K. S. Udell, J. Fluid Mech. **210**, 566 (1990).
[18] B. P. Ho and L. G. Leal, J. Fluid Mech. **71**, 361 (1975).
[19] T. M. Tsai and M. J. Miksis, J. Fluid Mech. **274**, 197 (1994).
[20] M. M. Dupin, I. Halliday, C. M. Care, L. Alboul, and L. L. Munn, Phys. Rev. E **75**, 066707 (2007).
[21] C. Sun and L. L. Munn, Biophys. J. **88**, 1635 (2005).
[22] P. Bagchi, Biophys. J. **92**, 1858 (2007).
[23] C. Pozrikidis, Phys. Fluids **17**, 031503(1) (2005).
[24] E. Jiang Ding and C. K. Aidun, Phys. Rev. Lett. **96**, 204502 (2006).
[25] J. M. Skotheim and T. W. Secomb, Phys. Rev. Lett. **98**, 078301 (2007).
[26] J. Beaucourt, F. Rioual, T. Seon, T. Biben, and C. Misbah, Phys. Rev. E **69**, 011906 (2004).
[27] T. Biben, K. Kassner, and C. Misbah, Phys. Rev. E **72**, 041921 (2005).
[28] A. Bilek, K. Dee, and D. Gaver, J. Appl. Physiol. **94**, 770 (2003).
[29] A. Jacob and D. Gaver, Phys. Fluids **17**, 031502 (2005).
[30] A. Esmaeeli and G. Tryggvason, J. Comput. Phys. **169**, 708 (2001).
[31] M. Sussman, A. Almgren, J. Bell, P. Colella, L. Howell, and M. Welcome, J. Comput. Phys. **148**, 81 (1999).
[32] R. Scardovelli and S. Zaleski, Annu. Rev. Fluid Mech. **31**, 576 (1999).
[33] A. J. James and J. Lowengrub, J. Comput. Phys. **201**, 685 (2004).
[34] M. Sussman and E. G. Puckett, J. Comput. Phys. **162**, 301 (2000).
[35] D. Jacqmin, J. Comput. Phys. **55**, 96 (1999).
[36] L. Lee and R. Leveque, SIAM J. Sci. Comput. (USA) **25**, 832 (2003).
[37] H. Udaykumar, R. Mittal, and W. Shyy, J. Comput. Phys. **153**, 535 (1999).
[38] J. Li, M. Hesse, J. Ziegler, and A. W. Woods, J. Comput. Phys. **208**, 289 (2005).
[39] S. Quan and D. P. Schmidt, J. Comput. Phys. **221**, 761 (2007).
[40] S. Chen and G. D. Doolen, Annu. Rev. Fluid Mech. **30**, 329 (1998).
[41] S. Mukherjee and J. Abraham, Phys. Rev. E **75**, 026701 (2007).
[42] S. V. Lishchuk, I. Halliday, and C. M. Care, Phys. Rev. E **77**, 036702 (2008).
[43] M. Sharan and A. S. Popel, Biorheology **38**, 415 (2001).
[44] Y. C. Fung, *Biomechanics: Circulation* (Springer-Verlag, New York, 1997).
[45] T. C. Papanastasiou, J. Rheol. **31**, 385 (1987).
[46] B. Das, P. C. Johnson, and A. S. Popel, Biorheology **37**, 239 (2000).
[47] P. S. Ayyaswamy, *Fluid Mechanics*, 4th ed. (Academic Press, Burlington, MA, 2008), Chap. 17, pp. 765–840.

[48] S. A. Berger, W. Goldsmith, and E. R. Lewis, *Introduction to Bioengineering* (Oxford University Press, New York, 1996).
[49] A. Pries, T. Secomb, and P. Gaehtgens, Pfluegers Arch. Eur. J. Physiol. **4401**, 653 (2000).
[50] M. Van Sint Annaland, W. Dijkhuizen, N. Deen, and J. Kuipers, AIChE J. **52**, 99 (2006).
[51] B. E. Griffith and C. S. Peskin, J. Comput. Phys. **208**, 75 (2005).
[52] G. Tryggvason, B. Bunner, A. Esmaeeli, D. Juric, N. Al-Rawahi, W. Tauber, J. Han, S. Nas, and Y. J. Jan, J. Comput. Phys. **169**, 708 (2001).
[53] P. Wesseling, *An Introduction to Multigrid Methods* (Wiley, New York, 1992).
[54] P. Colella, J. Comput. Phys. **87**, 171 (1990).
[55] S. Radl, G. Tryggvason, and J. G. Khinast, AIChE J. **53**, 1861 (2007).
[56] S. Shin and D. Juric, J. Comput. Phys. **180**, 427 (2002).
[57] S. Shin, S. I. Abdel-Khalik, V. Daru, and D. Juric, J. Comput. Phys. **203**, 493 (2005).
[58] F. Bretherton, J. Fluid Mech. **10**, 166 (1961).
[59] M. Heil, Phys. Fluids **13**, 2517 (2001).
[60] M. D. Giavedon and F. A. Saita, Phys. Fluids **9**, 2420 (1997).
[61] T. Haas and B. Duling, Microvasc. Res. **53**, 113 (1997).
[62] N. Vlahakis and R. Hubmayr, J. Appl. Physiol. **89**, 2490 (2000).
[63] P. Butler, T. Tsou, J. Li, S. Usami, and S. Chien, FASEB J. **15**, 216 (2001).
[64] H. Huang, R. Kamm, and R. Lee, Am. J. Physiol.: Cell Physiol. **287**, C1 (2004).
[65] P. McNeil and R. Steinhardt, J. Cell Biol. **137**, 1 (1997).
[66] J. Mendez, O. Rickman, and R. Hubmayr, Biol. Neonate **85**, 290 (2004).
[67] A. B. Branger and D. M. Eckmann, Anesthesiology **96**, 971 (2002).
[68] A. Suzuki, S. C. Armstead, and D. M. Eckmann, Anesthesiology **101**, 97 (2004).
[69] A. B. Branger and D. M. Eckmann, J. Appl. Physiol. **87**, 1287 (1999).
[70] S. C. Armstead and D. M. Eckmann, Anesthesiology **105**, 1220 (2006).